Supplement information for

Constraining anthropogenic CO_2 fluxes in mixed urban source areas using eddy covariance and footprint-informed ecological parameter migration

Jinwen Zhang[1,2], Yongjian Liang[2,3], Yufei Yang[1,2], Chenglei Pei[2,3], Hebiao Huang[4], Bo Huang[5], Xiufeng Lian[1,2], Yingyan Huang[2,3], Yuwen Peng[2,3], Chunlei Cheng[1,2], Cheng Wu[1,2], Zhen Zhou[1,2], and Mei Li[1,2]

[1]College of Environment and Climate, Institute of Mass Spectrometry and Atmospheric Environment, Guangdong Provincial Engineering Research Center for Online Source Apportionment System of Air Pollution, Guangdong–Hongkong–Macau Joint Laboratory of Collaborative Innovation for Environmental Quality, Jinan University, Guangzhou 511443, China

[2]Key Laboratory of Regional Air Quality Monitoring, Ministry of Ecology and Environment, Guangdong, Guangzhou 510308, China

[3]Guangzhou Ecological and Environmental Monitoring Center Station, Guangdong, Guangzhou 510006, China

[4]Guangzhou Academy of Agricultural and Rural Sciences, Guangdong, Guangzhou 510450, China

[5]Guangzhou Hexin Instrument Co., Ltd., Guangdong, Guangzhou 510530, China

Correspondence: Mei Li (limei@jnu.edu.cn)

S1. Quality-control procedure

To ensure that EC CO_2 fluxes could be used for subsequent storage correction, ecological-parameterization, and anthropogenic CO_2 flux estimation, we applied stepwise quality control to the 30 min flux data. The procedure is consistent with the flux processing described in Sect. 2.2 of the main text and includes removal of instrument and environmental anomalies, filtering of low-turbulence periods, stationarity testing, and despiking. The friction-velocity threshold (u*) was estimated following the standardized EC NEE post-processing framework of Papale et al. (2006) and its implementation in REddyProc (Wutzler et al., 2018). Table S1 reports the cumulative data-retention fraction after each step. The retention fractions in Table S1 are cumulative relative to the original 30 min records, not independent removal fractions for each step. After all quality-control steps, the final CO_2 flux data-retention fractions were 51.7 % at PY and 54.5 % at CH. This quality-controlled dataset was used to define the measured net CO_2 flux (F_{mz}), derive the storage-corrected net CO_2 flux (F_{cr}), fit ecological parameters, and partition the residual anthropogenic flux (F_{ff}) in the main text.

Table S1. Quality-control steps for EC CO_2 flux data and cumulative retention fractions.

Quality-control step	Filtering criterion	PY cumulative retention	CH cumulative retention	Process description	Relation to main-text analysis
Raw data	All 30 min EC CO_2 flux records	100 %	100 %	No filtering applied; only raw time-series organization was completed	Starting point for all quality control and subsequent flux calculation
Routine QC	Remove records flagged for instrument anomalies, extreme weather, maintenance, and obvious invalidity	91.6 %	97.1 %	Remove unreliable records caused by rainfall, instrument maintenance, abnormal diagnostic flags, and related issues	Ensure that data entering turbulence screening are not affected by obvious non-physical anomalies
Turbulence and EC-validity screening	Apply site- and season-specific u* thresholds; remove records failing stationarity, skew/spike, and statistical outlier checks	51.7 %	54.5 %	Remove 30 min fluxes affected by insufficient turbulent exchange or non-stationary/statistically anomalous EC conditions	Defines the quality-controlled EC flux dataset used to derive F_{mz} and F_{cr}; the u* threshold component is further evaluated in the sensitivity analysis

S2. Storage flux

Because CO_2 concentration measurements at additional heights were not available, storage flux was approximated from the temporal change in CO_2 concentration at the EC measurement height using a single-point approach (Hilland et al., 2025; Soininen et al., 2025). The storage flux below the measurement height was estimated by assuming a vertically uniform temporal change in CO_2 concentration, which simplifies the storage-flux calculation as follows (Aubinet et al., 2001; Papale et al., 2006; Kooijmans et al., 2017; Kohonen et al., 2020; Soininen et al., 2025):

$$F_{st} = \frac{P}{RT_a}\frac{dC}{dt}Z_m \qquad (S1)$$

Here F_{st} is the CO_2 storage flux (μmol m^{-2} s^{-1}), P is atmospheric pressure (Pa), T_a is air temperature (K), R is the molar gas constant (8.3144621 J K^{-1} mol^{-1}), Z_m is the EC measurement height (m), and dC/dt is the temporal change in CO_2 mole fraction. To reduce measurement-related noise, a standardized smoothing method was applied to concentration, using a 5 h moving average, equivalent to the mean of 10 consecutive data points (Soininen et al., 2025). Single-point storage estimates can be affected by vertical concentration gradients when the uniform-profile assumption is not fully met (Aubinet et al., 2001; Papale et al., 2006; Kooijmans et al., 2017). Previous analysis at a forest site suggested that this single-point storage approach may underestimate the storage flux by approximately 7 %, which is small relative to the measured flux magnitude (Kooijmans et al., 2017). We therefore applied a ± 10 % perturbation to the baseline storage flux as a slightly broader controlled sensitivity range to test how storage-correction uncertainty affects anthropogenic-flux estimation (Sect. S6).

S3. Human-respiration emissions

Because local hourly activity-intensity or mobile-signaling constraints were unavailable, we did not introduce an explicit activity-level function. Instead, we followed the simplified approach of Yang et al. (2025). The per-capita respiration rate CM was based on the range used by Zheng et al. (2023), varying from 120 μmol CO_2 cap^{-1} s^{-1} for the lowest activity level to 280 μmol CO_2 cap^{-1} s^{-1} for a higher activity level. It was linearly scaled according to the 24 h variation in population density. Population data were taken from the 2021 national hourly population-density spatial-distribution dataset, with a spatial resolution of 5 km × 5 km and population counts at 00:00, 08:00, 12:00, 16:00, and 20:00 (Xu, 2022). For PY and CH, population densities in the corresponding grid cells were extracted at these five times and linearly interpolated to construct continuous 24 h population-density series representing diurnal population changes in the site grid.

In the calculation, the gridded population count was first converted to areal population density:

$$P_h = \frac{D_h \times 10^4}{A_{grid}} \tag{S2}$$

Here P_h is the population density at hour h (cap m^{-2}), D_h is the population count in the grid cell at hour h (10^4 cap $grid^{-1}$), and Agrid is the area of a 5 km × 5 km grid cell. The hourly per-capita respiration rate was then calculated according to the amplitude of diurnal population-density variation:

$$C_M(h) = C_{M,min} + \frac{P_h - P_{min}}{P_{max} - P_{min}}\left(C_{M,max} - C_{M,min}\right) \tag{S3}$$

Here C_M (h) is the per-capita CO_2 respiration rate at hour h (μmol CO_2 cap^{-1} s^{-1}), $C_{M,min}$ is 120 μmol CO_2 cap^{-1} s^{-1}, $C_{M,max}$ is 280 μmol CO_2 cap^{-1} s^{-1}, and P_{max} and P_{min} are the maximum and minimum population densities within the 24 h period at the site (cap m^{-2}). The human-respiration CO_2 flux was then calculated as:

$$F_{hu}(h) = P_h \times C_M(h) \tag{S4}$$

Here F_{hu} (h) is the human-respiration CO_2 flux at hour h (μmol m^{-2} s^{-1}). This method follows the population-density × per-capita-respiration framework of Zheng et al. (2023) and adopts the simplified treatment of Yang et al. (2025) for cases lacking more detailed activity data. The resulting hourly flux therefore reflects both population changes and part of the diurnal variation in activity intensity. Because human presence and activity intensity within the EC footprint are only approximated by gridded population density and a scaled per-capita respiration rate, ±50 % perturbations of the baseline human-respiration flux were used as a conservative sensitivity range in Sect. S6.

S4. Calculation of PAR and VPD

Photosynthetically active radiation (PAR) was not measured directly in this study and was therefore estimated from measured shortwave radiation (Sect. S7). Following common practice in ecosystem carbon-flux and light-use-efficiency studies, we assumed that approximately 45 %

of incoming shortwave radiation falls within the photosynthetically active waveband and used the photon-energy conversion factor of 4.57 μmol J^{-1} to convert shortwave radiation to PAR (McCree, 1972; Akitsu et al., 2022):

$$PAR(t) = R_g(t) \times 0.45 \times 4.57 \tag{S5}$$

Here PAR (t) is photosynthetically active radiation at time t (μmol photon m^{-2} s^{-1}), and R_g (t) is total shortwave radiation (W m^{-2}). In flux partitioning, nighttime ecosystem-respiration fitting used PAR < 10 μmol photon m^{-2} s^{-1} as the criterion for no photosynthetic activity, while daytime GPP light-response fitting mainly used samples with relatively strong radiation and satisfying the other quality-control criteria.

Because CH shortwave radiation was obtained from an auxiliary station about 19 km from the EC tower, its local representativeness was treated as a potential input uncertainty. The CH-only ±10 % shortwave-radiation perturbation was used to cover possible donor-site radiation-input differences associated with station separation and unresolved cloud-field heterogeneity. Previous studies have shown that cloud-induced shortwave-radiation variability can reach the order of 10 % or more over 10–20 km scales, especially under heterogeneous or broken-cloud conditions (Song et al., 2016; Madhavan et al., 2017). The CH-only perturbations were therefore included in Sect. S6 to test how this input uncertainty propagates into CH-side ecological parameters and PY residual anthropogenic flux, rather than to define an instrument-specific confidence interval.

Vapor pressure deficit (VPD) was used to characterize atmospheric dryness and to drive the VPD inhibition term in the GPP structural sensitivity experiment. Given air temperature Ta and relative humidity RH, saturation vapor pressure was calculated using the Tetens equation (Allen et al., 1998):

$$e_s\big(T_a(t)\big) = 0.6108\, exp\left(\frac{17.27\, T_a(t)}{T_a(t) + 237.3}\right) \tag{S6}$$

Here e_s is saturation vapor pressure (kPa), and Ta is air temperature (°C). Actual vapor pressure was then calculated as:

$$e_a(t) = \left(\frac{RH(t)}{100}\right) e_s\big(T_a(t)\big) \tag{S7}$$

Here e_a is actual vapor pressure (kPa), and RH is relative humidity expressed as a percentage from 0 to 100 %. VPD was then calculated as:

$$VPD(t) = e_s(T_a(t)) - e_a(t) = e_s(T_a(t))\left(1 - \frac{RH(t)}{100}\right) \quad (S8)$$

All VPD values are reported in kPa. To avoid non-physical values, negative VPD values were set to 0 after calculation. In this study, PAR mainly serves as the radiation driver of the GPP light-response model. It is used for the saturating + VPD inhibition sensitivity experiment in Sect. 2.4 and for interpreting the eco-meteorological background in Figs. S6–S7.

S5. Footprint-weighted land cover, EVI, and bottom-up emission inventories

The source area of EC observations changes at half-hourly scales with wind direction, turbulence intensity, atmospheric stability, and boundary-layer conditions. Land cover or EVI within a fixed-radius buffer therefore cannot fully represent the actual flux source area at each observation time. To reduce this source-area representativeness bias, we combined two-dimensional flux-footprint weights with high-resolution land-cover (10 m) and HLS EVI data (30 m; 2–3 day) to construct time-step-resolved footprint-weighted land-cover fractions and footprint-weighted EVI (Zhang et al., 2025; Neigh, 2021; Neigh, 2025).

For each half-hourly observation time t, the footprint model first provided the relative contribution weight of each grid cell in the study domain to the tower flux. The footprint weights satisfy:

$$\sum\nolimits_{i,j} w_{ij}\,(t) = 1 \quad (S9)$$

The global 10 m land-cover raster was then registered to the same coordinate system and grid as the footprint field. For land-cover class c, an indicator function $I_{c,ij}$ was defined as 1 when pixel ij belonged to class c and 0 otherwise. The footprint-weighted land-cover fraction at time t was then calculated as:

$$LD_{c,fp}(t) = \frac{\sum_{i,j} w_{ij}(t) I_{c,ij} M_{ij}}{\sum_{i,j} w_{ij}(t)\, M_{ij}} \quad (S10)$$

Here $LD_{c,fp}$ (t) is the contribution fraction of land-cover class c within the footprint at time t, dimensionless and ranging from 0 to 1, and M_{ij} is the valid land-cover mask, equal to 1 when pixel ij has a valid land-cover classification and 0 otherwise. The main classes used here are vegetation, impervious surface, and water/wetland, which support interpretation of source-area differences in net CO_2 flux and residual anthropogenic CO_2 flux.

EVI data were taken from Harmonized Landsat Sentinel-2 (HLS) L30 and S30 vegetation-index products. Because HLS observations are affected by clouds, cloud shadows, aerosols, and satellite revisit frequency, high-quality observations are not available for every pixel on every day. We first applied quality control to HLS L30 and S30, removing clouds, cloud shadows, low-quality pixels, and anomalous EVI values. Valid observations from the two sensors were then merged to build continuous EVI time series. For each pixel, observations were sorted by date. When no high-quality EVI observation was available on a given day, the nearest valid observation was used to construct a daily continuous series. If the gap between preceding and following valid observations was short, linear interpolation was further applied to reduce step-like changes caused by discrete satellite sampling.

For any time t, footprint-weighted EVI was calculated as:

$$EVI_{fp}(t) = \frac{\sum_{i,j} w_{ij}(t) EVI_{ij}(t) M_{ij}(t)}{\sum_{i,j} w_{ij}(t)\, M_{ij}(t)} \quad (S11)$$

Here $EVI_{ij}(t)$ is the EVI value of pixel ij on the date corresponding to time t, and $M_{ij}(t)$ is the valid EVI mask, equal to 1 when the pixel has valid EVI and 0 otherwise. This weighting uses only valid EVI pixels and renormalizes the footprint weights over valid pixels. If the fraction of valid EVI pixels within the footprint was below the preset threshold at a given time, the EVI estimate was flagged as low-confidence and was not prioritized for parameter migration or sensitivity analysis.

Two EVI time-window settings were used. The baseline was a 3 d window: for flux observation date d, the nearest quality-controlled valid HLS EVI observation within d ± 3 d was searched first. If multiple valid observations were available within the window, the temporally closest observation was preferred, and linear interpolation between preceding and following valid observations was applied when needed to obtain EVI for date d. This stricter setting reduces vegetation-state errors caused by long temporal extrapolation and was therefore used as the baseline for CH-to-PY parameter migration.

The sensitivity setting used a 5 d window. With all other processing unchanged, the search range for the nearest valid EVI observation was relaxed to d ± 5 d. This setting increases effective EVI coverage, especially during cloudy, rainy, or HLS-sparse periods. Its potential cost is that EVI may represent vegetation conditions farther from the flux-observation date. The 5 d window was therefore not used as the baseline, but as an EVI input sensitivity experiment to evaluate how EVI temporal-continuity treatment affects parameter migration and anthropogenic flux.

Three bottom-up inventories for 2023 were selected for comparison with contemporaneous observation-inferred results: ODIAC2024 (1 km × 1 km), EDGAR2024 (0.1° × 0.1°), and MEIC-global-CO_2 v1.0 (0.1° × 0.1°) (Oda et al., 2018; Crippa et al., 2024; Xu et al., 2024). All three inventories were processed into monthly mean area fluxes consistent with monthly footprint climatologies and converted to μmol m^{-2} s^{-1}. After monthly inventory flux fields were obtained, the inventory grids were mapped onto the same grid as the monthly footprint climatology, and the footprint-weighted monthly inventory value for the site was calculated as:

$$E_{fp,m} = \frac{\sum_i w_{i,m} E_{i,m}}{\sum_i w_{i,m}} \qquad (S12)$$

Here $E_{fp,m}$ is the footprint-weighted inventory flux in month m (μmol m^{-2} s^{-1}), $E_{i,m}$ is the inventory flux of pixel i in month m, and $w_{i,m}$ is the relative contribution weight of pixel i to the tower flux under the monthly footprint climatology. The summation was performed over valid footprint pixels. For higher-resolution inventories such as ODIAC, the inventory field was directly resampled to the footprint grid before weighting. For coarser inventories such as EDGAR and MEIC, the grid cell containing the site and neighboring grid cells were used to construct a local inventory field before mapping to the footprint grid, reducing representativeness bias that could arise if the tower were close to a coarse-grid boundary. The final footprint-weighted inventory results were used to provide a monthly magnitude context and a diagnostic of spatial-allocation plausibility for the observation-constrained anthropogenic CO_2 flux, rather than to strictly validate any inventory product.

S6. Uncertainty analysis

The uncertainty analysis used a design consisting of a baseline scheme, single-factor perturbations, and structural alternatives. The scenarios do not represent equally probable outcomes; they are used to test the sensitivity of anthropogenic CO_2 flux to key inputs, ecological-parameter migration, and model-structure choices. The scenario settings are listed in Table S2.

The final propagation ensemble included 14 CH-side scenarios combined with 3 human-respiration scenarios, producing 42 propagation combinations. The u*, storage-flux, and EVI scenarios require synchronized changes in CH-side parameter construction and PY-side inputs to avoid inconsistency between donor parameters and target-site drivers. The ±10 % and ±20 % u* perturbations were used as controlled sensitivity ranges because u* threshold selection is a major uncertainty in EC post-processing and is commonly evaluated using bootstrap-derived threshold distributions or multiple threshold scenarios (Papale et al., 2006; Wutzler et al., 2018). The CH-only radiation scenarios perturb only the CH-side shortwave-radiation input and are used specifically to evaluate how donor-site radiation representativeness affects migrated parameters. The CH radiation-input and storage-flux ±10 % perturbations should be interpreted as controlled sensitivity ranges, not as instrument-specific confidence intervals; their rationale is described in Sects. S4 and S2, respectively. Similarly, the ±50 % human-respiration perturbations were used to represent uncertainty in gridded population density, footprint-scale human presence, and activity-dependent per-capita respiration, rather than as a formal confidence interval.

Table S2. Uncertainty propagation scenario settings.

Scenario family	Scenario ID	Setting	Main target tested	Synchronized with PY inputs
Baseline	CH0	Baseline u*, baseline storage flux, 3 d EVI, temperature-stratified saturating GPP structure, and baseline daytime-respiration inhibition	Main result	Yes
u* threshold	CH1	Baseline seasonal u* threshold −20 %	Effect of weak-turbulence filtering on NEE and parameter fitting	Yes
u* threshold	CH2	Baseline seasonal u* threshold −10 %	Effect of weak-turbulence filtering on NEE and parameter fitting	Yes
u* threshold	CH3	Baseline seasonal u* threshold +10 %	Effect of weak-turbulence filtering on NEE and parameter fitting	Yes
u* threshold	CH4	Baseline seasonal u* threshold +20 %	Effect of weak-turbulence filtering on NEE and parameter fitting	Yes

Storage flux	CH5	Baseline storage flux −10 %	Uncertainty in single-point storage correction	Yes
Storage flux	CH6	Baseline storage flux +10 %	Uncertainty in single-point storage correction	Yes
EVI time window	CH7	EVI search window relaxed from 3 d to 5 d	Temporal representativeness and coverage of remotely sensed EVI	Yes
GPP structure	CH8	Pure saturating light-response structure; no temperature stratification or VPD inhibition; all GPP fitting samples use one parameter group for α, P_{max}, and θ	GPP model-structure uncertainty	Yes
GPP structure	CH9	Saturating light response + VPD inhibition; VPD inhibition parameter determined by fitting	Whether the VPD inhibition term provides additional explanatory power	Yes
Temperature grouping	CH10	Alternative temperature grouping Scheme B, expanding the mid-temperature group by 0.5 °C toward both low and high temperatures	Uncertainty in temperature-stratification boundary selection	Yes
Respiration structure	CH11	Weak daytime-respiration inhibition; lower the light-inhibition strength relative to the baseline while keeping other settings unchanged	Uncertainty in daytime-respiration inhibition strength	Yes
CH radiation input	CH12	CH-side shortwave-radiation input −10 % only; PY-side radiation input kept at baseline	Effect of CH radiation-input representativeness on ecological-parameter migration	No; CH side only
CH radiation input	CH13	CH-side shortwave-radiation input +10 % only; PY-side radiation input kept at baseline	Effect of CH radiation-input representativeness on ecological-parameter migration	No; CH side only
Human respiration	human base	Baseline human-respiration emissions	Additive non-fossil CO_2 term	Added independently
Human respiration	human low50	0.5 × baseline human respiration	Sensitivity to under- or overestimation of human respiration	Added independently
Human respiration	human high50	1.5 × baseline human respiration	Sensitivity to under- or overestimation of human respiration	Added independently

S7. Auxiliary monitoring information

PY shortwave solar radiation, NO_x, and $PM_{2.5}$ observations were obtained from the Higher Education Mega Center atmospheric-environment monitoring station, located about 2 km northeast of the PY tower. Both sites are within the university-town community and inside the ring road network of Guangzhou Higher Education Mega Center. CH shortwave solar-radiation observations were obtained from the Conghua Tianhu atmospheric-environment monitoring station, located about 19 km southwest of the CH tower. Other high-precision greenhouse-gas measurements (CO_2/CO) and meteorological variables were measured at the two EC sites. Figure S6 shows that shortwave radiation at CH and PY has a similar seasonal phase, supporting the consistency of regional radiation background.

Because CH radiation was not measured in situ at the tower, however, its representativeness was still treated as a potential input uncertainty and propagated using the CH12–CH13 CH-only ±10 % radiation perturbations in Table S2, with the perturbation rationale described in Sect. S4. By contrast, PY radiation was obtained from a nearby station within the university-town area and was not considered the dominant radiation-representativeness risk in this study. The CH-only perturbations were designed specifically to test donor-site radiation-input representativeness.

S8. Road-traffic congestion data and traffic-activity indicators

To help interpret the morning and evening peaks and directional differences in anthropogenic CO_2 flux (F_{ff}) at PY, we introduced road-traffic congestion data around the PY site as auxiliary evidence for spatiotemporal traffic-activity variation (https://lbs.amap.com/api/webservice/guide/api/trafficstatus, last access: 25 May 2026). The road-traffic data cover the major roads within about 1.5 km of the PY tower. The raw data are hourly snapshots of road status, with attributes including road geometry, observation time, and road-congestion level. The monitoring period was from 23:00:00 on 6 May 2026 to 13:00:00 on 24 May 2026, including 331 hourly road-status snapshots, 117047 road records, and 713 unique road segments. The records were nearly continuous over this period, with only a small number of missing hourly snapshots or road-status records.

The road-congestion data were collected in May 2026 and do not fully overlap with the main EC analysis period of 2023–2024. The data are therefore not used for hourly matched validation of EC fluxes or for conversion to traffic CO_2 emission fluxes. They are used only to characterize typical diurnal and directional patterns of road-traffic activity around the PY university-town area. To assess the reasonableness of using asynchronous congestion data as auxiliary indicators of typical traffic-activity patterns, we followed the logic of Yang et al. (2025) regarding campus population stability and further examined public information on population size and traffic-management background for the main campus activity sources around PY. The surrounding area is mainly Guangdong University of Technology. Public information from the university shows that student enrollment exceeded 54000 in 2024 and, including international students, exceeded 55000 in 2025 (https://fzghc.gdut.edu.cn, last access: 25 May 2026), indicating only a small increase in student population. Public traffic-management notices show that requirements for low-speed vehicle operation, pedestrian priority, vehicle registration, visitor-vehicle reporting, and regulated parking have been continuously enforced in recent years (https://bwc.gdut.edu.cn/info/1137/1810.htm, last access: 25 May 2026). Public information does not indicate any major change between 2024 and 2026 in the road layout around the university-town campus, campus-gate access rules, or parking infrastructure that would be sufficient to reshape diurnal traffic patterns. We therefore treat the May 2026 road-congestion data as asynchronous auxiliary traffic-activity indicators, not as synchronous validation data for 2023–2024 EC fluxes.

The road-congestion variable traffic ranges from 1 to 5: 1 indicates free flow, 2 slow traffic, 3 congestion, 4 severe congestion, and 5 missing data. Because traffic = 5 does not represent a real congestion state but missing or special road status, it was excluded from calculations of mean congestion index, congestion fraction, and cumulative congestion load. Its frequency and spatial distribution were recorded separately. Valid road-status levels include only traffic = 1–4.

Road-vector data from different times were first merged into a long table. Stable road-segment identifiers (segment_id) were constructed from road geometry coordinates to avoid bias caused by changes in record ordering among snapshots. The length L_i of each road segment was calculated from its geometry, where i denotes the ith road segment. For the whole road area around PY, the hourly length-weighted mean congestion index was defined as:

$$T_h = \frac{\sum_{i=1}^{M_h} L_i T_{i,h}}{\sum_{i=1}^{M_h} L_i} \qquad (S13)$$

Here T_h is the regional mean congestion index at hour h, $T_{i,h}$ is the valid congestion level (1–4) of road segment i at hour h, L_i is segment length, and M_h is the number of road segments with valid status records at hour h. This metric was used to analyze the 24 h variation in road-traffic status and to compare it with the morning and evening peak structure of PY anthropogenic CO_2 flux. To characterize the persistence and cumulative intensity of segment-level congestion, cumulative congestion load for each segment was calculated as:

$$CB_i = \sum_{t=1}^{N_i} max(T_{i,t} - 1, 0) \qquad (S14)$$

Here CB_i is the cumulative congestion index for road segment i, with units that can be expressed as index hours, and N_i is the number of valid observations for that segment. This metric treats free-flow status (traffic = 1) as zero congestion contribution, while slow, congested, and severely congested traffic correspond to congestion increments of 1, 2, and 3, respectively. It therefore captures both congestion intensity and duration for a given segment. In addition to the mean congestion index, we calculated the fraction of road length with slow or worse traffic, congestion or worse traffic, and severe congestion, corresponding to traffic ≥ 2, traffic ≥ 3, and traffic = 4 as fractions of total valid road length. These fractions help determine whether the spatial extent of congested roads expands during different periods.

To align the traffic analysis with flux source areas and wind-sector analysis, the azimuth angle of each road-segment center relative to the PY tower was calculated, and roads were divided into eight directional sectors: N, NE, E, SE, S, SW, W, and NW. Azimuth was defined as 0° at north and increased clockwise, with sectors divided at 45° intervals. For any hour h and directional sector s, the sector-level length-weighted mean congestion index was calculated as:

$$T_{h,s} = \frac{\sum_{i \in s} L_i T_{i,h}}{\sum_{i \in s} L_i} \qquad (S15)$$

Here $T_{h,s}$ is the mean congestion index for directional sector s at hour h. This metric was used to construct an hour × directional-sector congestion heat map, to determine which directions contributed most to morning- or evening-peak traffic enhancement, and to compare with wind-sector differences in PY anthropogenic CO_2 flux, NO_x/CO/CO_2/$PM_{2.5}$ diurnal patterns, and impervious-surface source-area distribution.

Road-congestion level cannot be directly converted into CO_2 emission flux because vehicle type, traffic volume, speed, emission factor, and road capacity are not available in this dataset. We therefore do not use the road-congestion data as a traffic-emission inventory. Instead, we use them only as independent auxiliary evidence for the spatiotemporal distribution of traffic activity. Hourly diurnal variation is used to test whether traffic activity has morning and evening peak structures similar to F_{ff}. Eight-sector congestion load and hour-sector heat maps are used to identify the directions in which traffic enhancement occurs. Road-segment spatial distribution is used to identify specific road segments responsible for sectoral congestion differences.

Table S3. Summary of climate and ecological conditions at the CH and PY sites.

Metric	CH donor site	PY target site	Implication for the CH-to-PY parameter-migration assumption
Climate zone	Humid subtropical monsoon climate of Guangzhou	Humid subtropical monsoon climate of Guangzhou	Supports shared regional seasonal forcing, but does not imply identical microclimate
Air temperature	Similar seasonal phase to PY; generally cooler	Similar seasonal phase to CH; generally warmer	Supports shared seasonal temperature forcing, while indicating non-identical urban and suburban microclimates
VPD	Similar seasonal magnitude to PY; month-to-month consistency relatively weak	Similar seasonal magnitude to CH; month-to-month consistency relatively weak	Indicates broadly comparable atmospheric dryness, with larger short-term or site-specific differences than temperature and radiation
Daytime shortwave radiation	Similar seasonal phase to PY	Similar seasonal phase to CH	Supports comparable radiation seasonality for light-response migration; radiation-input uncertainty is evaluated separately
Dominant vegetation background	High vegetation cover, dominated by urban forest/evergreen broadleaf species	Urban green space coexisting with evergreen broadleaf urban-forest patches	Supports using the CH ecological response as a same-region, broadly similar vegetation-type reference
Footprint land cover	High vegetation fraction and very low impervious-surface fraction	Mixture of vegetation, impervious surface, and water bodies	Shows that PY cannot directly use CH fluxes or unscaled parameters; footprint constraints are required
EVI_{fp} seasonal phase	Higher in summer and lower in winter and spring	Higher in summer and lower in winter and spring	Supports a similar phenological background at the two sites
EVI_{fp} magnitude	Overall higher	Overall lower	Supports EVI_{fp}-based scaling of capacity-type parameters
Anthropogenic influence	Weak	Strong	Supports CH as an ecological-parameter donor and PY as a mixed urban target source area

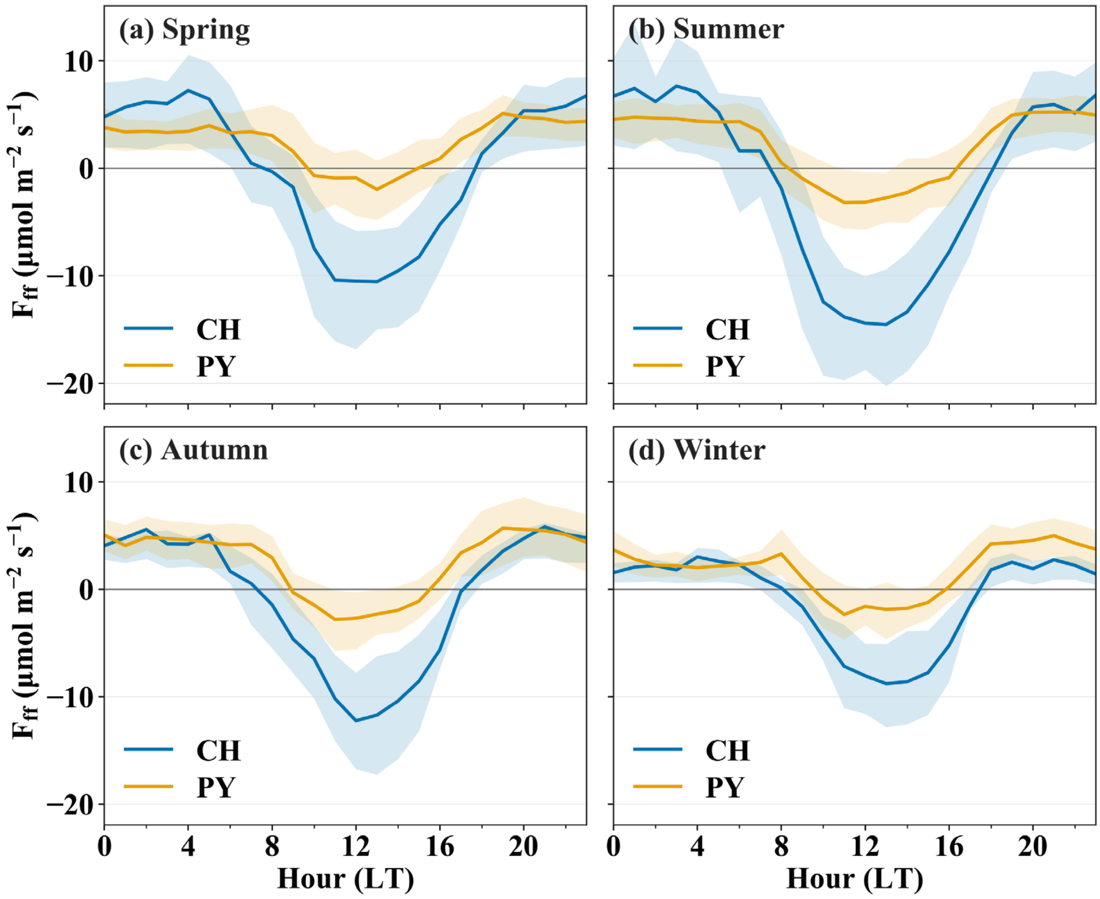

Figure S1. Seasonal diurnal cycles of corrected CO_2 flux (F_{cr}) at the PY and CH sites. Hourly mean F_{cr} is shown separately for **(a)** spring (March–May), **(b)** summer (June–August), **(c)** autumn (September–November), and **(d)** winter (December–February). Lines represent the mean diurnal cycle, and shaded bands indicate the interquartile range (Q25–Q75). Positive values indicate net CO_2 release to the atmosphere, whereas negative values indicate net uptake.

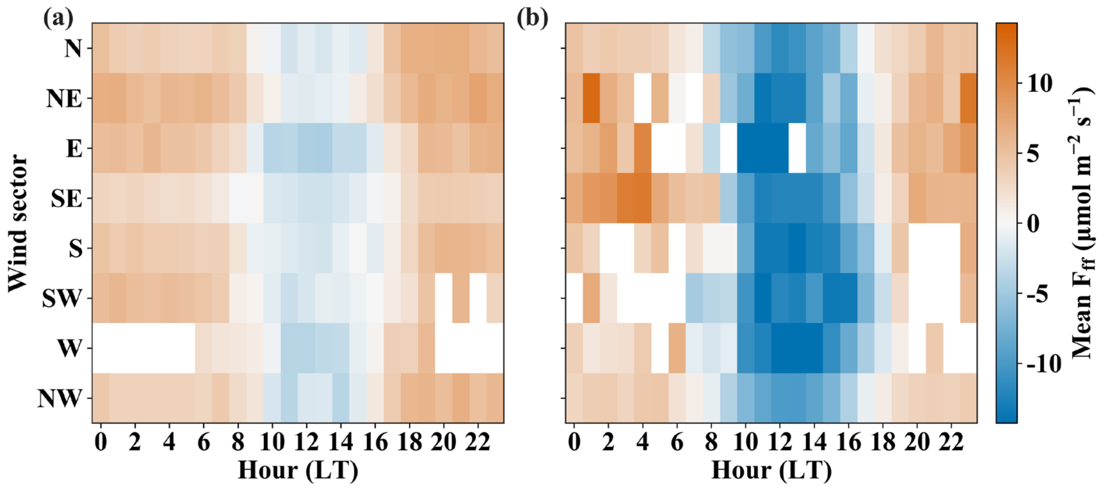

Figure S2. Sector-hour heatmaps of corrected CO_2 flux (F_{cr}) at the **(a)** PY and **(b)** CH sites. Each grid cell represents the mean hourly F_{cr} for a given wind sector and hour of day in local time. Cells with fewer than 5 valid hourly records are masked in white.

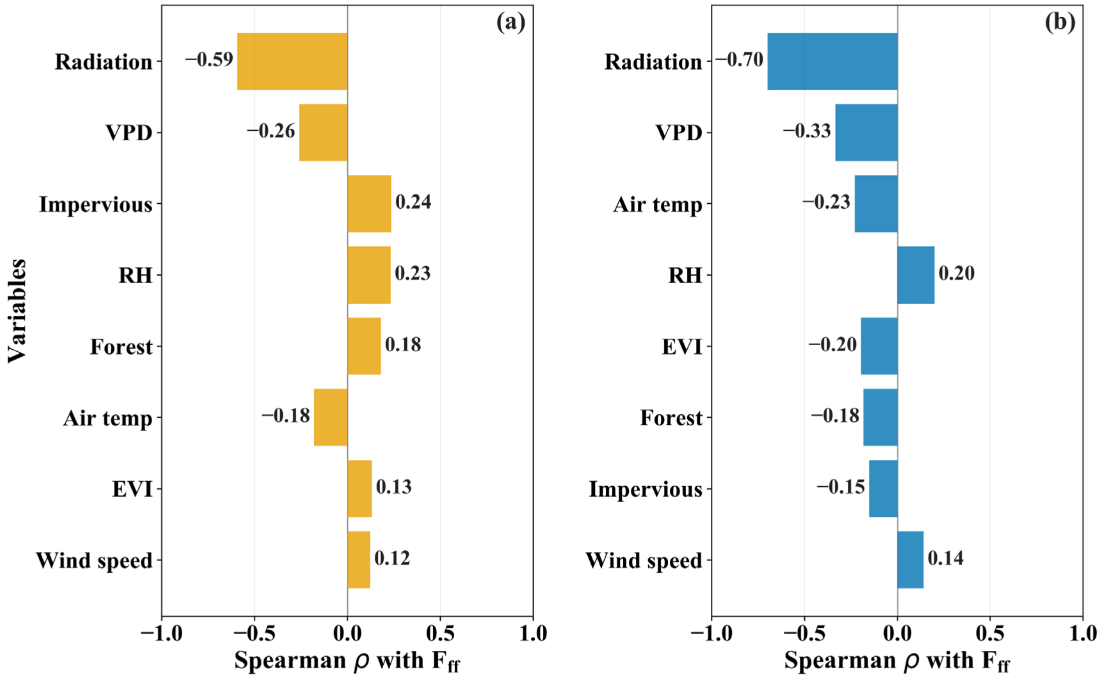

Figure S3. Correlations between corrected CO_2 flux (F_{cr}) and environmental or land-cover variables at the **(a)** PY and **(b)** CH sites. Bars indicate Spearman correlation coefficients computed from hourly data in 2023–2024.

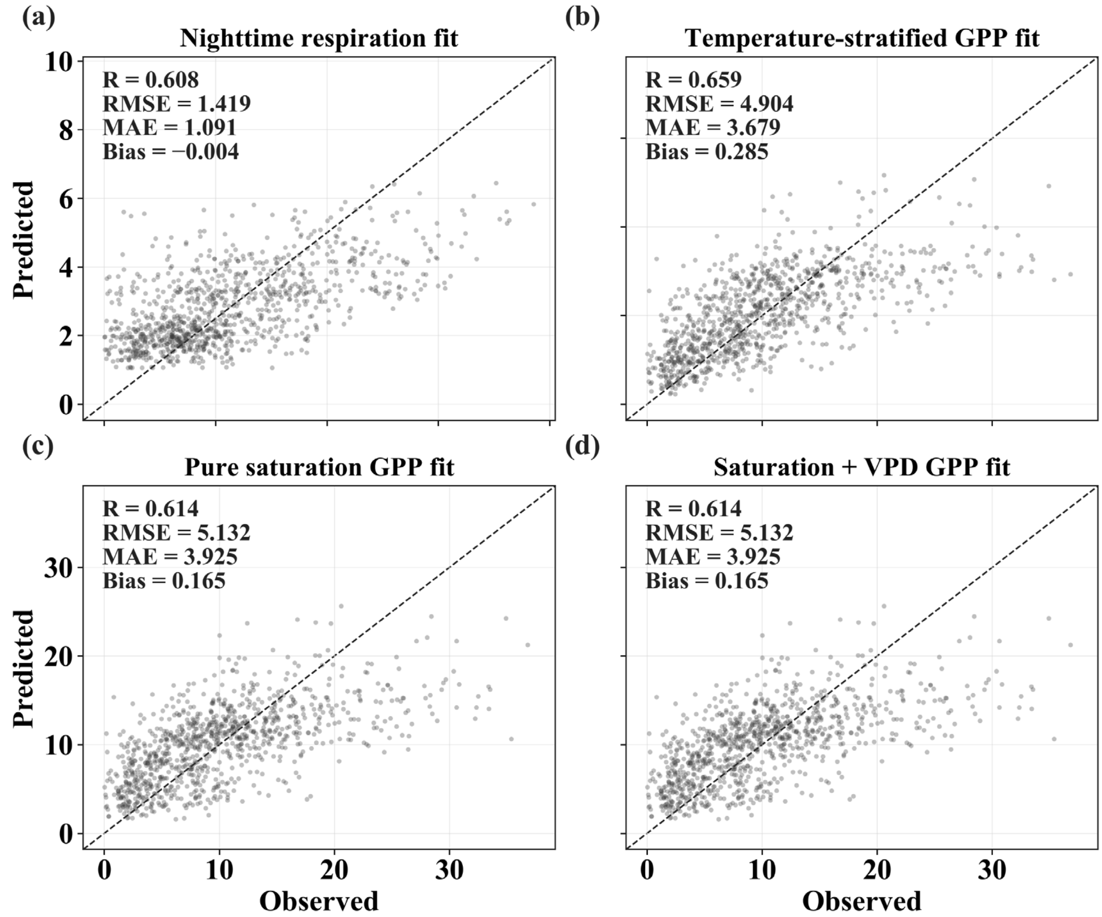

Figure S4. Fitted-versus-observed diagnostics for the CH respiration and GPP models. Panel **(a)** shows the main-case nighttime respiration fit, panel **(b)** shows the main-case temperature-stratified GPP fit, panel **(c)** shows the pure saturation GPP fit, and panel **(d)** shows the saturation plus VPD GPP fit. Dashed lines indicate the 1:1 relationship; inset metrics summarize R, RMSE, MAE, and bias.

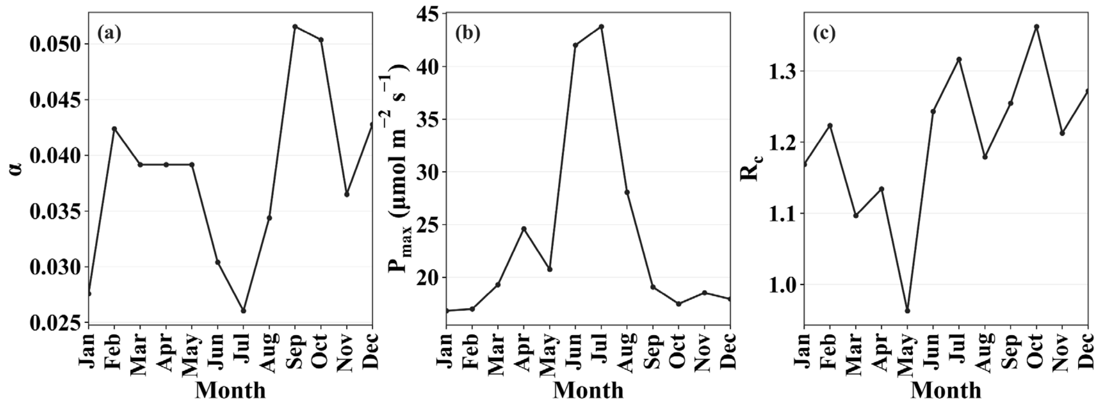

Figure S5. Monthly variation of CH donor-site ecological parameters used for footprint-constrained parameter migration. Monthly medians of the smoothed CH donor parameters for **(a)** the initial light-use efficiency α, **(b)** the maximum photosynthetic capacity P_{max}, and **(c)** the fitted base respiration coefficient R_c. α and P_{max} were derived from GPP parameter days, whereas R_c was derived from respiration parameter days.

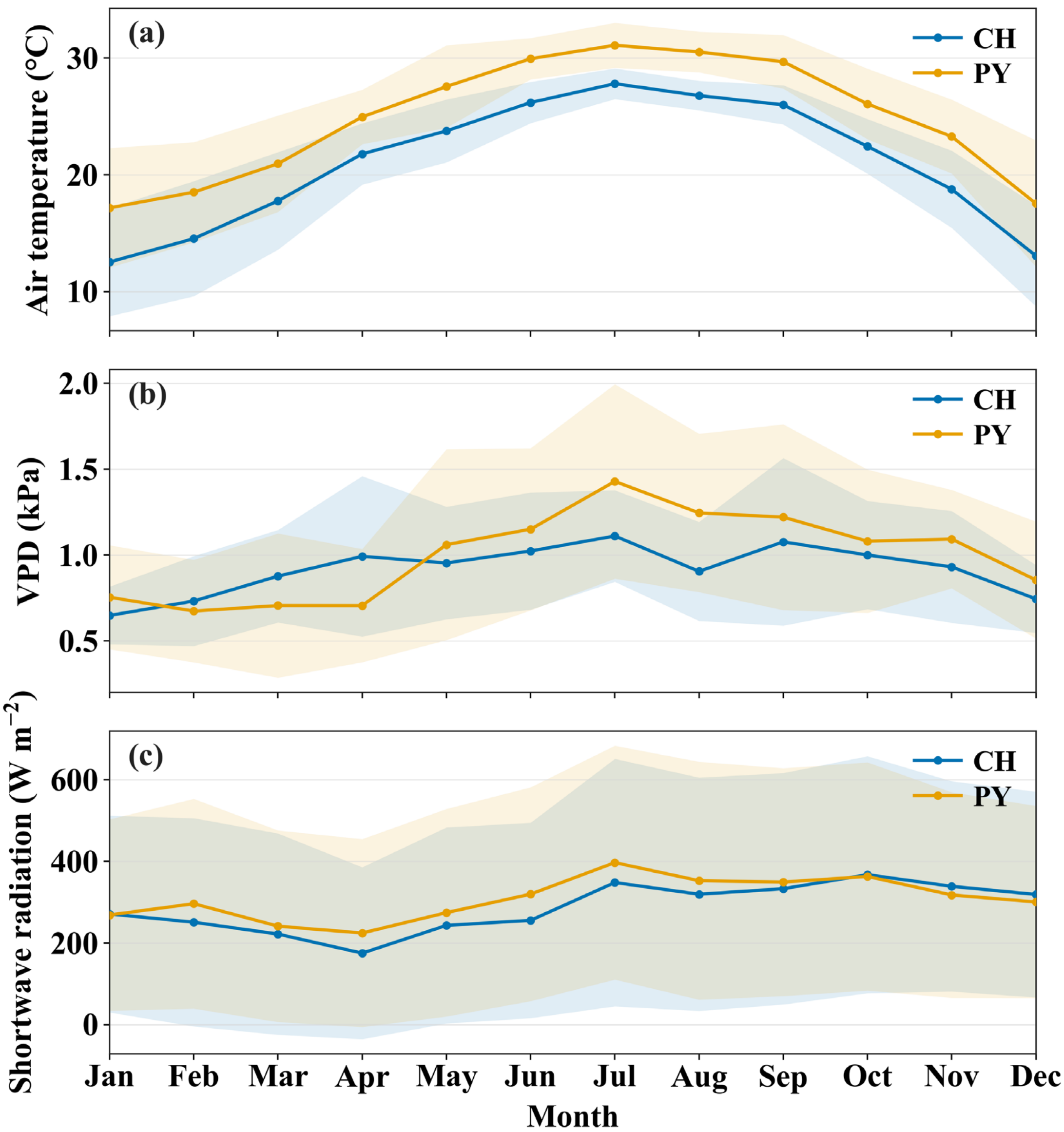

Figure S6. Seasonal environmental background at the CH donor site and PY target site. Calendar-month mean **(a)** air temperature, **(b)** vapor pressure deficit (VPD), and **(c)** daytime shortwave radiation at CH and PY based on available records from 2023–2024. Lines show calendar-month means and shaded bands indicate ±1 standard deviation.

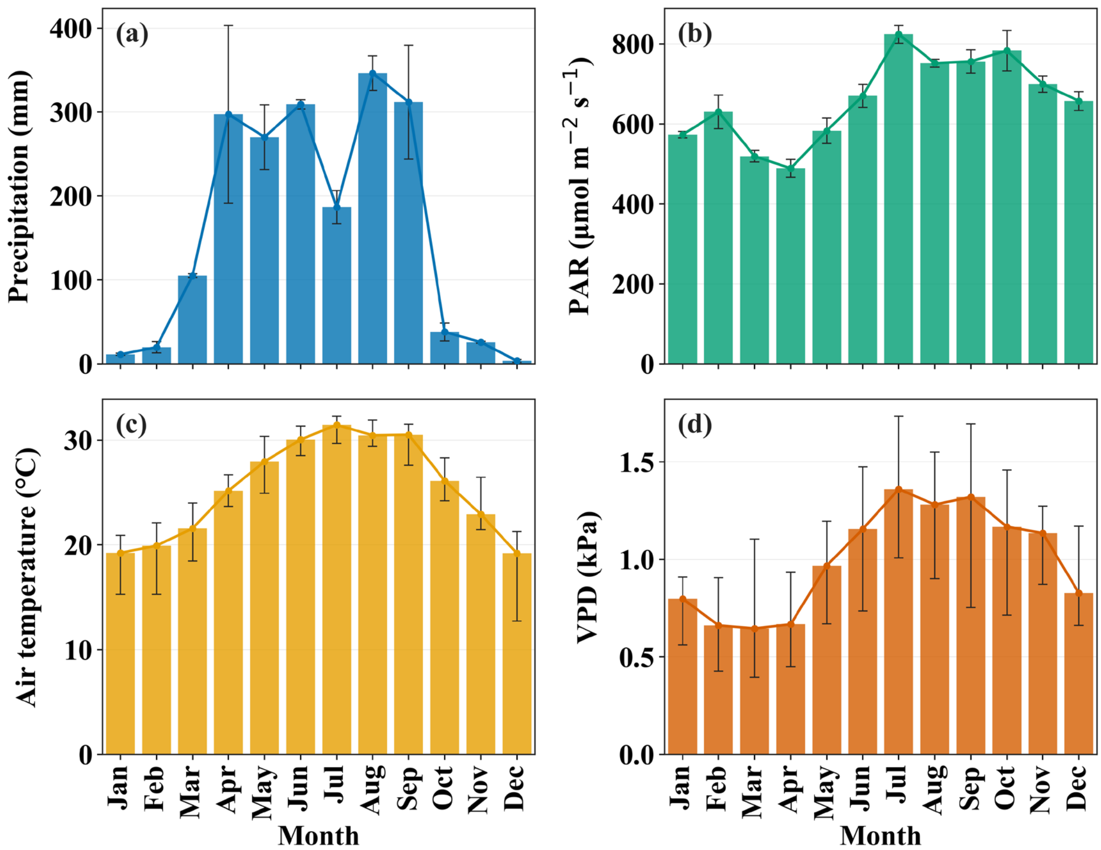

Figure S7. Monthly hydroclimatic and radiation conditions at the PY site during 2023–2024. **(a)** Monthly cumulative precipitation, **(b)** daytime mean PAR proxy, **(c)** daily mean air temperature, and **(d)** daily mean vapor pressure deficit (VPD). Bars show the median of monthly or daily-derived values grouped by calendar month, and error bars indicate the interquartile range (Q25–Q75).

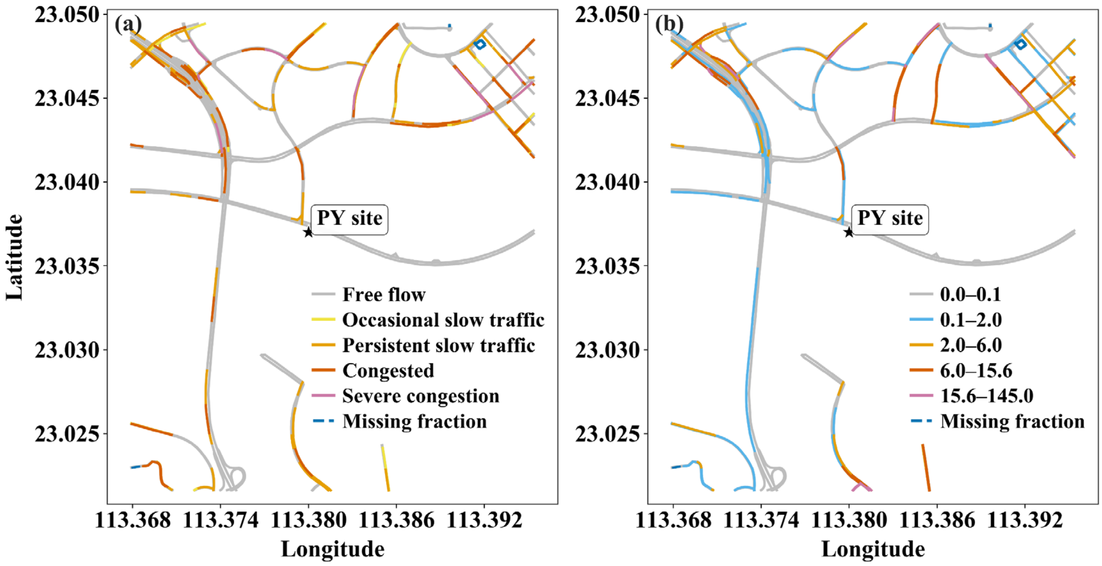

Figure S8. Spatial distribution of traffic congestion characteristics around the PY site. **(a)** Road segments classified by the segment-level mean congestion class. **(b)** Road segments classified by the cumulative congestion burden, defined as the sum of (traffic − 1) for records with traffic levels from 1 to 4.

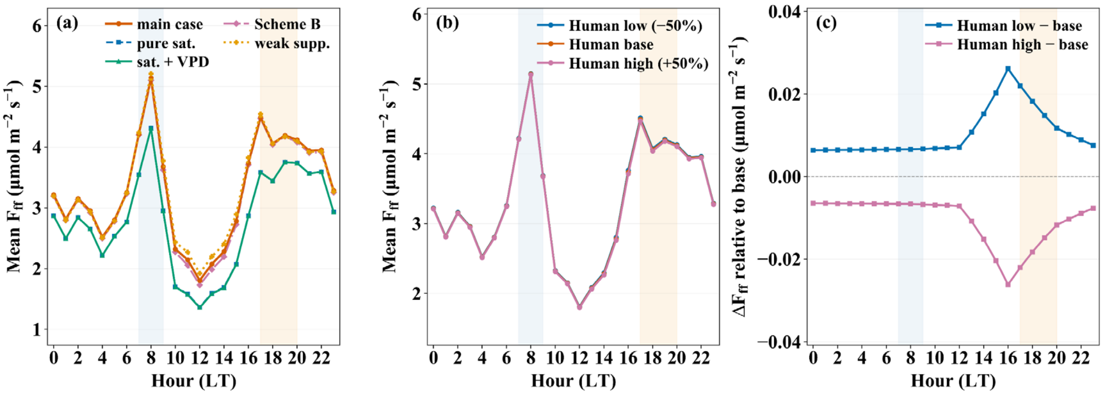

Figure S9. Sensitivity of the PY anthropogenic CO_2 flux (F_{ff}) to core structural assumptions and human-respiration magnitude. **(a)** Diurnal mean F_{ff} under the five core structural scenarios, including the main case, pure saturation, saturation + VPD, Scheme B, and weak daytime suppression, all shown under the base human-respiration setting. **(b)** Diurnal mean F_{ff} in the main case under three human-respiration settings (−50 %, base, and +50 %). **(c)** Diurnal difference in F_{ff} relative to the human-base case for the low and high human-respiration settings.

References

Akitsu, T. K., Nasahara, K. N., Ijima, O., Hirose, Y., Ide, R., Takagi, K., and Kume, A.: The variability and seasonality in the ratio of photosynthetically active radiation to solar radiation: A simple empirical model of the ratio, International Journal of Applied Earth Observation and Geoinformation, 108, 102724, https://doi.org/10.1016/j.jag.2022.102724, 2022.

Allen, R. G., Pereira, L. S., Raes, D., and Smith, M.: Crop evapotranspiration-Guidelines for computing crop water requirements-FAO Irrigation and drainage paper 56, FAO, http://www.fao.org/3/X0490E/x0490e00.htm#Contents, 300, D05109, 1998.

Aubinet, M., Chermanne, B., Vandenhaute, M., Longdoz, B., Yernaux, M., and Laitat, E.: Long term carbon dioxide exchange above a mixed forest in the Belgian Ardennes, Agr. Forest Meteorol., 108, 293-315, https://doi.org/10.1016/S0168-1923(01)00244-1, 2001.

Crippa, M., Guizzardi, D., Pagani, F., Banja, M., Muntean, M., Schaaf, E., Monforti-Ferrario, F., Becker, W. E., Quadrelli, R., Risquez Martin, A., Taghavi-Moharamli, P., Köykkä, J., Grassi, G., Rossi, S., Melo, J., Oom, D., Branco, A., San-Miguel, J., Manca, G., Pisoni, E., Vignati, E., and Pekar, F.: GHG emissions of all world countries, Publications Office of the European Union, https://doi.org/10.2760/4002897, 2024.

Hilland, R., Hashemi, J., Stagakis, S., Brunner, D., Constantin, L., Kljun, N., Kunz, A. K., Molinier, B., Hammer, S., Emmenegger, L., and Christen, A.: Sectoral attribution of greenhouse gas and pollutant emissions using multi-species eddy covariance on a tall tower in Zurich, Switzerland, Atmos. Chem. Phys., 25, 14279-14299, https://doi.org/10.5194/acp-25-14279-2025, 2025.

Kohonen, K. M., Kolari, P., Kooijmans, L. M. J., Chen, H., Seibt, U., Sun, W., and Mammarella, I.: Towards standardized processing of eddy covariance flux measurements of carbonyl sulfide, Atmos. Meas. Tech., 13, 3957-3975, https://doi.org/10.5194/amt-13-3957-2020, 2020.

Kooijmans, L. M. J., Maseyk, K., Seibt, U., Sun, W., Vesala, T., Mammarella, I., Kolari, P., Aalto, J., Franchin, A., Vecchi, R., Valli, G., and Chen, H.: Canopy uptake dominates nighttime carbonyl sulfide fluxes in a boreal forest, Atmos. Chem. Phys., 17, 11453-11465, https://doi.org/10.5194/acp-17-11453-2017, 2017.

Madhavan, B. L., Deneke, H., Witthuhn, J., and Macke, A.: Multiresolution analysis of the spatiotemporal variability in global radiation observed by a dense network of 99 pyranometers, Atmos. Chem. Phys., 17, 3317-3338, https://doi.org/10.5194/acp-17-3317-2017, 2017.

McCree, K. J.: Test of current definitions of photosynthetically active radiation against leaf photosynthesis data, Agricultural meteorology, 10, 443-453, https://doi.org/10.1016/0002-1571(72)90045-3, 1972.

Neigh, C.: HLS Operational Land Imager Vegetation Indices Daily Global 30m v2.0, NASA Land Processes Distributed Active Archive Center [dataset], https://doi.org/10.5067/HLS/HLSL30_VI.002, 2025.

Neigh, C., Ju, J., Roger, J.-C., Skakun, S., Vermote, E., Claverie, M., Dungan, J., Yin, Z., Freitag, B., and Justice, C.: HLS Sentinel-2 Multi-spectral Instrument Surface Reflectance Daily Global 30m v2.0, NASA Land Processes Distributed Active Archive Center [dataset], https://doi.org/10.5067/HLS/HLSS30.002, 2021.

Oda, T., Maksyutov, S., and Andres, R. J.: The Open-source Data Inventory for Anthropogenic

CO_2, version 2016 (ODIAC2016): a global monthly fossil fuel CO_2 gridded emissions data product for tracer transport simulations and surface flux inversions, Earth Syst. Sci. Data, 10, 87-107, https://doi.org/10.5194/essd-10-87-2018, 2018.

Papale, D., Reichstein, M., Canfora, E., Aubinet, M., Bernhofer, C., Longdoz, B., Kutsch, W., Rambal, S., Valentini, R., and Vesala, T.: Towards a more harmonized processing of eddy covariance CO_2 fluxes: algorithms and uncertainty estimation, Biogeosciences, 3, 571–583, https://doi.org/10.5194/bg-3-571-2006, 2006.

Soininen, J., Kohonen, K.-M., Rantala, P., Kulmala, L., Aaltonen, H., and Järvi, L.: Carbon uptake of an urban green space inferred from carbonyl sulfide fluxes, npj Clim. Atmos. Sci., 8, 90, https://doi.org/10.1038/s41612-025-00958-5, 2025.

Song, S., Schmidt, K. S., Pilewskie, P., King, M. D., Heidinger, A. K., Walther, A., Iwabuchi, H., Wind, G., and Coddington, O. M.: The spectral signature of cloud spatial structure in shortwave irradiance, Atmos. Chem. Phys., 16, 13791-13806, https://doi.org/10.5194/acp-16-13791-2016, 2016.

Wutzler, T., Lucas-Moffat, A., Migliavacca, M., Knauer, J., Sickel, K., Šigut, L., Menzer, O., and Reichstein, M.: Basic and extensible post-processing of eddy covariance flux data with REddyProc, Biogeosciences, 15, 5015-5030, https://doi.org/10.5194/bg-15-5015-2018, 2018.

Xu, R., Tong, D., Xiao, Q., Qin, X., Chen, C., Yan, L., Cheng, J., Cui, C., Hu, H., and Liu, W.: MEIC-global-CO_2: A new global CO_2 emission inventory with highly-resolved source category and sub-country information, Sci. China Earth Sci, 67, 450-465, https://doi.org/10.1007/s11430-023-1230-3, 2024.

Xu, X.: National hourly population density spatial distribution dataset, Resource and Environmental Science Data Registration and Publication System [dataset], https://doi.org/10.12078/2022091601, 2022.

Yang, S., Kong, F., Yin, H., Zou, J., Järvi, L., and Sun, J.: Short-term responses of urban forest carbon dynamics to combined heatwave and drought in subtropical China, Agr. Forest Meteorol., 372, 110728, https://doi.org/10.1016/j.agrformet.2025.110728, 2025.

Zhang, X., Liu, L., Zhao, T., Zhang, W., Guan, L., Bai, M., and Chen, X.: GLC_FCS10: a global 10 m land-cover dataset with a fine classification system from Sentinel-1 and Sentinel-2 time-series data in Google Earth Engine, Earth Syst. Sci. Data, 17, 4039-4062, https://doi.org/10.5194/essd-17-4039-2025, 2025.

Zheng, Y., Havu, M., Liu, H., Cheng, X., Wen, Y., Lee, H. S., Ahongshangbam, J., and Järvi, L.: Simulating heat and CO_2 fluxes in Beijing using SUEWS V2020b: sensitivity to vegetation phenology and maximum conductance, Geosci. Model Dev., 16, 4551-4579, https://doi.org/10.5194/gmd-16-4551-2023, 2023.